X International Conference on Computational Methods for Coupled Problems in Science and Engineering
COUPLED PROBLEMS 2023
M. Papadrakakis, B. Schrefler and E. Oñate (Eds)

A NUMERICAL APPROACH FOR THE CHARACTERIZATION OF THE FREE-FALL DYNAMICS OF THIN DISKS

A. Lolli* **and G. Corsi***

*The BioRobotics Institute, Scuola Superiore Sant'Anna, Pisa
e-mail: alberto.lolli@santannapisa.it

Key words: Non linear dynamics, Coupled Problems, Numerical simulations, Computational Fluid Dynamics

Abstract. This study focuses on investigating numerically the dynamics of thin disks freely falling inside viscous and incompressible fluids. We solve the model by using the finite element method and the main falling modes are identified using the Reynolds number and dimensionless inertia moment. The results are mapped in a phase diagram for comparison with existing literature and validation of the simulations. The effect of introducing a hole in the disk geometry is investigated, analyzing variations in trajectories and Strouhal numbers. Furthermore, falling styles are quantified by examining the fluctuations of the orientation of the axis of the disks over time. Additionally, a quantitative analysis of the solid body velocities for the fluttering and tumbling modes highlights the significant differences between them. The study successfully characterizes the main falling modes through qualitative and quantitative analyses.

1 INTRODUCTION

The phenomenon of bodies with different densities moving in a surrounding fluid presents complex behaviors, which can be observed in everyday examples such as falling leaves from trees or air bubbles rising in water. Predicting the trajectories of these bodies is highly challenging since we can retrieve chaotic behavior. In the literature, various types of trajectories have been reported, including steady falling, periodic oscillation, tumbling, and seemingly chaotic motion [7],[8]. Even bodies with simple geometries can exhibit a wide range of behaviors, further adding to the complexity of understanding and predicting their motions. The study of such dynamical systems requires coupling the motion equations for the solid body with those of the surrounding fluid. Due to the complexity and non-linearity of these equations, exact solutions are generally unattainable without simplified assumptions about solid geometry and fluid regimes. Therefore, numerical simulations provide a valuable tool for a better understanding of those complex systems [3] and consequently, they find extensive application in various engineering fields, ranging from aeronautics to geophysics. Direct Numerical Simulations (DNS) have the potential to fully resolve the equations governing fluid dynamics across all temporal and spatial scales without the need for turbulence models, thus providing a higher degree of accuracy. However, this approach incurs a significant computational cost, and the utilization of supercomputers is required. We had the advantage of utilizing the high-performance computing facilities at CINECA, which provided us with efficient computational resources and capabilities. In this

study, we focused on the dynamics of thin disks freely falling inside viscous and incompressible fluids. To facilitate our research we studied geometries which possess axial symmetry along the vertical axis represented by the unit vector e_z fixed in the body frame, meaning that their appearance remains unchanged when rotated around this axis. This symmetry simplifies the study of the solid body dynamics, as the moments of inertia along the horizontal axes (x and y) are equal and the inertia tensor becomes diagonal under these geometric assumptions. We opted for corrugated board as the solid material, which has an approximate density of 100 $\frac{kg}{m^3}$. This choice allows us to explore a wide range of non-dimensional moment of inertia. An estimation of the descent velocity of the disks is analytically determined based on the balance between the drag force, gravity, and buoyancy. This velocity is then utilized a-priori to calculate the fluid dynamics regime using the Galileo number, which directly influences the viscosity of the fluid. Subsequently, the fluid regimes are identified a-posteriori using the Reynolds number, employing the descent velocity obtained from simulation data, ranging from 18 to 800 and compared with that a-priori. We mapped out our results in a phase diagram using fluid dynamics regime and geometric information, this has allowed us to compare the different falling modes with those already documented in the literature e.g. [4] and will serve in the future to validate the simulations with real experiments. The stabilizing effect of a hole is defined as the transition from a mode where predicting the object's landing point is highly difficult to one where it becomes more predictable, [6]. We have investigated the effect of introducing a hole in the geometry observing variations in the trajectories and in the Strouhal numbers for a qualitative and quantitative analysis. Finally we show the fluctuations of the e_z unit vector over time and the velocities profiles for tumbling and fluttering, to quantify the falling styles and confirm the qualitative results on the trajectories.

2 MODEL

In our simulations, particular attention was given to the following parameters:

$$\begin{cases} \rho = \dfrac{\rho_s}{\rho_f} \\ \chi = \dfrac{d_o}{h} \\ U_t = \sqrt{|\rho - 1| h g (d_o - d_i)} \\ G = \dfrac{U_t d_o}{\nu} \\ \nu = \dfrac{U_t (d_{out} - d_{in})}{G} \\ I^* = \rho \dfrac{\pi}{64\chi} \left(1 - \left(\dfrac{d_i}{d_o}\right)^4\right) \\ Re = U_m \dfrac{d_o - d_i}{\nu} \end{cases} \tag{1}$$

Here, $\rho_{s,f}$ represents the densities of the solid and fluid phases, respectively. The parameter χ quantifies the aspect ratio of the body, with $d_{i,o}$ denoting the inner/outer diameter of the disc and h representing its height. The terminal velocity U_t is determined using an a-priori formula which enters in the Galileo number G, while ν denotes the fluid viscosity. The dimensionless inertia moment is denoted by I^*, which depends on ρ and the ratio of d_i to d_o. The Reynolds number Re is defined in terms of the mean simulated terminal velocity U_m and the difference

in diameters $(d_o - d_i)$, normalized by the fluid viscosity ν. The simulation model couples two distinct physical phenomena: the fluid dynamics surrounding the object and the dynamics of the solid body $\mathcal{B}$. This enables the simulation of a fluid-structure interaction problem within a volume $\mathcal{V}_f$ occupied by a viscous and incompressible fluid. If we consider the motion of a solid body inside an inviscid fluid we can write the Kirchhoff's equations describing the linear and angular momentum balance as follows:

$$\begin{cases} (m\mathbb{I} + \mathbb{A})\dfrac{d\mathbf{U}}{dt} + \boldsymbol{\Omega} \times ((m\mathbb{I} + \mathbb{A})\mathbf{U}) = 0 \quad on\ \mathcal{B} \\ \\ (\mathbb{J} + \mathbb{B})\dfrac{d\boldsymbol{\Omega}}{dt} + \boldsymbol{\Omega} \times ((\mathbb{J} + \mathbb{B})\boldsymbol{\Omega}) + \mathbf{U} \times (\mathbb{A}\mathbf{U}) = 0 \quad on\ \mathcal{B} \end{cases} \tag{2}$$

Where the inertia tensor of the body is denoted as $\mathbb{J}$, while tensors $\mathbb{A}$ and $\mathbb{B}$ represent the added mass and inertia contributions to the solid body, respectively.
In the present study, we denote the fluid fields using $\mathbf{v}$ and p, while the linear and angular velocities of the solid body are represented by $\boldsymbol{U} = [u_1, u_2, u_3]^T$ and $\boldsymbol{\Omega} = [\omega_1, \omega_2, \omega_3]^T$, respectively. The position vector $\mathbf{r}$ is defined with respect to the center of mass of the body.

$$\begin{cases} m\mathbb{I}\dfrac{d\mathbf{U}}{dt} + \boldsymbol{\Omega} \times (m\mathbb{I}\mathbf{U}) = \mathbf{F}_{fl}(\mathbf{v}, p) + (m - \rho_f \mathcal{V}_s)\mathbf{g} \quad on\ \mathcal{B} \\ \\ \mathbb{J}\dfrac{d\boldsymbol{\Omega}}{dt} + \boldsymbol{\Omega} \times (\mathbb{J}\boldsymbol{\Omega}) = \mathbf{M}_{fl}(\mathbf{v}, p) \quad on\ \mathcal{B} \\ \\ \frac{\partial}{\partial t}\rho_f + \nabla \cdot (\rho_f \mathbf{v}) = 0 \quad in\ \mathcal{V}_f/\mathcal{B} \\ \\ \frac{\partial}{\partial t}\rho_f \mathbf{v} + \boldsymbol{\Omega} \times \mathbf{v} + \rho_f([\mathbf{v} - (\boldsymbol{U} + \boldsymbol{\Omega} \times \mathbf{r})] \cdot \nabla)\mathbf{v} = -\nabla p + \mu\Delta\mathbf{v} + \mathbf{F}_{vol} \quad in\ \mathcal{V}_f/\mathcal{B} \end{cases} \tag{3}$$

The first two equations describe the linear and angular conservation of the momentum for $\mathcal{B}$ considering the effect of viscosity and vorticity in the first right-hand terms, while the second two are the Navier-Stokes written with respect to a reference system that is integral with the body and projected into a fixed one whose axes rotate like the principal axes of inertia of the solid. This allows to avoid the remeshing of the fluid zone saving on the computational time. The coupling is achieved through two mechanisms. First, terms derived from the stress tensor generated by the fluid velocity field are inserted into the equations governing the motion of the solid body. Second, boundary conditions are imposed on the surface of the object to account for the interaction with the fluid. Terms F_{fl}, M_{fl} account for the contributions from the fluid stresses acting on the body computed through:

$$\begin{cases} \mathbf{F}_{fl} = \displaystyle\int_{\partial\mathcal{B}} \mu\mathbb{D}\mathbf{n} + p\mathbb{I} \quad d\Sigma \\ \\ \mathbf{M}_{fl} = \displaystyle\int_{\partial\mathcal{B}} (\mu\mathbb{D}\mathbf{n} + p\mathbb{I})(\mathbf{r} \times \mathbf{n}) \quad d\Sigma \end{cases} \tag{4}$$

where $\mathbb{D}$ is the strain rate tensor. The calculation of the added mass components, which are used to model the inertial response of the fluid to the accelerations of a body, i.e. during the

time variation of $\mathbf{U}$, $\mathbf{\Omega}$, considering only the pressure contributions modelled using potential flow theory, is done starting from the relationship:

$$F_i = M_{ij} a_j \tag{5}$$

where M_{ij} is the diagonal added mass tensor and a_{ij} are the instantaneous solid acceleration components, indeed due to above hypothesis we can say that the induced velocity v_i in the fluid is linear with solid velocity components $U_j = [u_1, u_2, u_3, \omega_1, \omega_2, \omega_3]^T$. Indexes $i, j = 1, 2, \ldots, 6$ refer to a unitary translation (rotation) of the body in the x, y, z directions:

$$v_i = u_{ij} U_j \tag{6}$$

where

$$u_{ij} = \frac{\partial \phi_j}{\partial x_i} \tag{7}$$

and ϕ is the potential of the steady flow. Then to assemble the mass matrix one has to consider the following integrals over the body surface:

$$M_{ij} = -\rho_f \int_{\partial \mathcal{B}} \phi_i \frac{\partial \phi_j}{\partial n} \quad d\Sigma. \tag{8}$$

we solve this at the beginning of each simulation by using potential flow approximation with $u_j = 1$ for $j = 1, \ldots, 6$ and $u_{i \neq j} = 0$. The calculated fluid fields will be reused to compute the correction to the fluid solution at each time step due to changes in the boundary conditions on the surface of the body corresponding to instantaneous solid accelerations. These fields and the added mass matrix will be instrumental in our procedure to solve the coupling in (3), which is based on the approach described in [1]. A finite element algorithm was carried out using the FEniCS library [11] to solve the Navier-Stokes equations, imposing the following boundary conditions at the contact region between the fluid and the solid, as well as at the computational walls:

$$\begin{cases} \mathbf{v} \cdot \mathbf{n} = (\mathbf{U} + \mathbf{\Omega} \times \mathbf{r}) \cdot \mathbf{n} & \text{on } \partial \mathcal{B} \\ \mathbf{v} = \mathbf{0} & \text{on } \partial \mathcal{V}_f \end{cases} . \tag{9}$$

As documented in [5], the fractional step method employed in this study is described by the following set of equations:

$$\frac{\mathbf{v}^I - \mathbf{v}^{n-1}}{\Delta t} + B^{n-1/2} = \nu \nabla^2 \left(\frac{\mathbf{v}^I - \mathbf{v}_i^{n-1}}{2} \right) - \nabla p^* + f^{n-1/2} \tag{10}$$

$$\nabla^2 \varphi = -\frac{1}{\Delta t} \nabla \cdot \mathbf{v}^I \tag{11}$$

$$\frac{\mathbf{v}^n - \mathbf{v}^I}{\Delta t} = -\nabla \varphi \tag{12}$$

In the above equations, φ represents the corrected pressure, and p^* corresponds to the tentative pressure. The unknown tentative velocity, $\mathbf{v}^I$, is solved for in the first equation, and the

non-linear convective term is linearized using the matrix B, computed at the midpoint between two consecutive time instances employing a second-order accurate scheme. For the numerical solution of the ODEs related to the solid body dynamics, the Radau method is utilized. This is achieved through the use of the *integrate.solve_ivp* function. The following pseudo algorithm outlines the workflow of the developed code:

Algorithm 1 FSI falling disks pseudo-algorithm

Set t=0
Set U(t) = [0,0,0,0,0,0]^T
$M_{ij} \leftarrow$ Solve (8)
while t $\leq T_f$
Set bcs (9) using U^{n-1}, Ω^{n-1}
$t = t^n = t^{n-1} + \Delta t$
    while iter $\leq$ **max iter** & **residuals** $\geq$ **max error**
    Set $\phi = p^*$
    $v_i^I \leftarrow$ Solve (10)
    $p^{n-1/2} \leftarrow$ Solve (11)
    Set $\phi = p^{n-1/2} - \phi$
    end
  $v_i^n \leftarrow$ Solve (12)
F_{fl}^n, $M_{fl}^n \leftarrow$ Solve (4)
U^n, $\Omega^n \leftarrow$ Solve first 2 eqs in (3)
Update fluid variables with superposition
end

3 RESULTS

In this section, we present the results of our study in both qualitative and quantitative manners. Figure 1 illustrates a section of the computational domain, highlighting the configurations of both perforated and full disks.

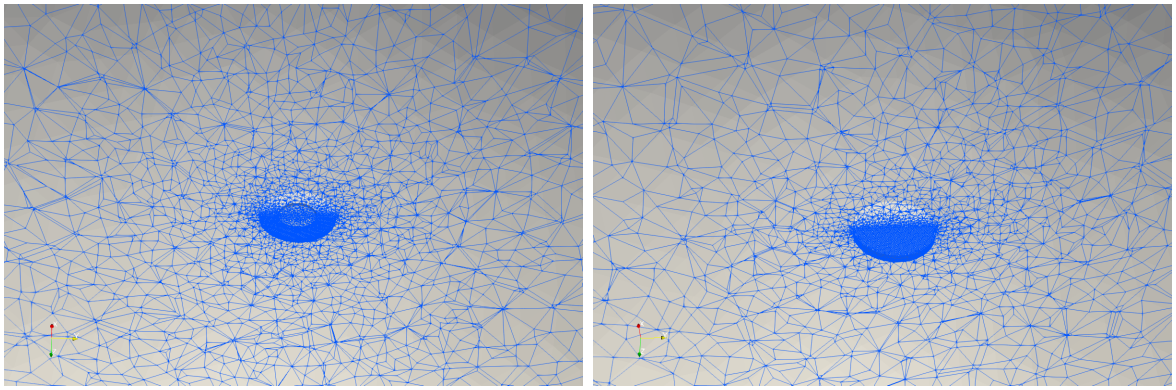

Figure 1: Computational mesh around the discs

We have identified and classified the main falling styles exhibited by thin discs of several dimensions and thickness, both for perforated and full configurations. In the following figures, we present visual representations of the different trajectories, including the steady state, weakly oscillating, fluttering, helicoidal tumbling, and tumbling. These experiments refer to the disks with dimensionless inertia moment and Reynolds reported in tables 1 and 2. For what concern the thickness-to-ratio parameter, all the modes have $\chi = 50$ except the fourth which has $\chi = 10$. In the perforated disk cases the inner diameter is chosen to be half the outer one. Visualizing those modes allows us to gain qualitative insights into the dynamics of these objects during free fall.
As expected, at low Reynolds numbers, we observe a straight trajectory for the falling objects. However, as the Reynolds number increases, oscillations start to appear due to the emergence of instabilities. This is why we refer to the second mode in figure 2 as the weakly oscillating regime. Keeping unchanged the dimensionless moment of inertia and increasing the number of Re we have a shifting towards the fluttering from the weakly oscillation mode. We call the second mode in figure 3 helicoidal tumbling because the disk strongly deviates from the vertical and autorotates on itself following a helicoidal trajectory.
At higher reynolds number we recover the typical tumbling mode and also a choatic trajectory is found. The Strouhal number, which is a dimensionless parameter that represents the frequency of vortex detachment, was calculated for all the modes, except the chaotic one. It is possible to compute the Strouhal number by using oscillation frequency f associated to U_x in the laboratory frame, using the mean velocity U_m of the disk from simulation data, hence:

$$St = \frac{f(d_o - d_i)}{U_m} \tag{13}$$

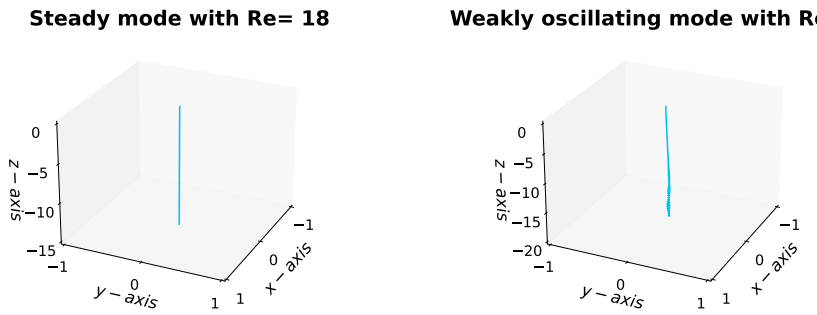

Figure 2: Steady and weakly oscillating trajectories

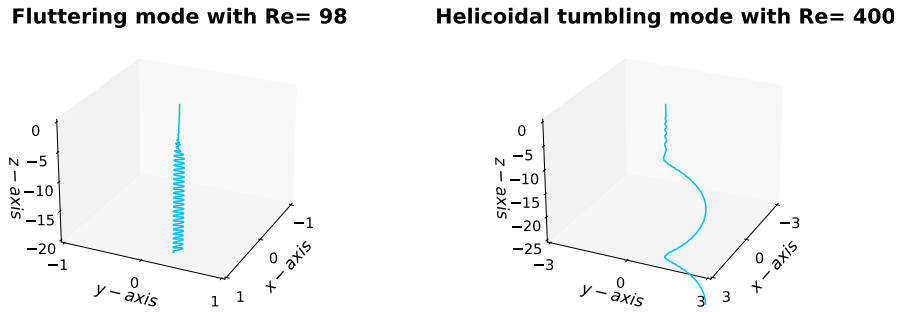

Figure 3: Fluttering and helicoidal tumbling trajectories

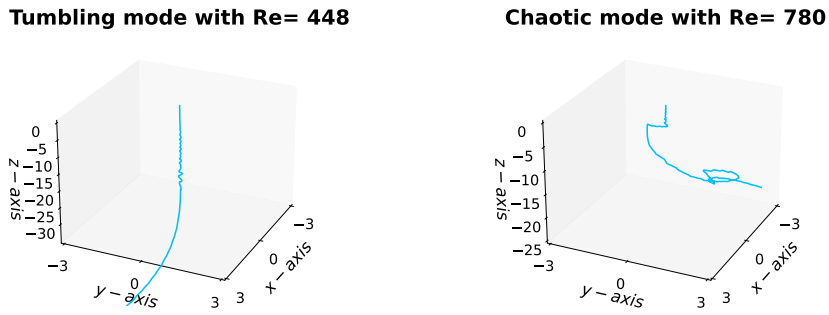

Figure 4: Tumbling and chaotic trajectories

I^*	Re	Mode	St
0.0751	18	Steady oblique	0
0.0751	48	Weakly oscillating	0.0591
0.0751	268	Fluttering	0.1258
0.3755	400	Helicoidal tumbling	0.2501

Table 1: Strouhal number for perforated disks

I^*	Re	Mode	St
0.0801	36	Steady oblique	0
0.0801	96	Fluttering	0.1718
0.0801	448	Tumbling	0.4404
0.205	780	Chaotic	-

Table 2: Strouhal number for full disks

Upon analyzing the values for both configurations, it becomes apparent that there is a decrease in the Strouhal number when the disk is perforated. This trend can be interpreted as a stabilization process, likely attributable to a reduction in the moment of inertia. However, it is possible that there exists an additional stabilizing contribution resulting from vortices generated within the inner hole. These vortices may act as a counterbalance to the external vortices, further contributing to the overall stabilization. Summarizing, the falling styles in a phase diagram as in Fig. 5 allows us to immediately have an indication of the trajectory expected by an object from the knowledge of only two parameters, one for the solid and one for the fluid. Further results, including the determination of the critical values of inertia and Reynolds number beyond which the steady falling style is unstable are given in [12].

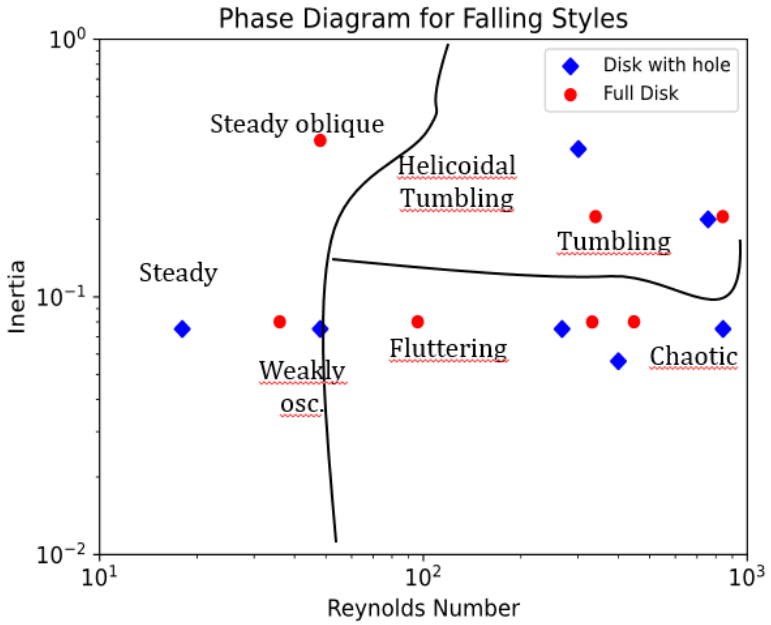

Figure 5: Phase diagram for falling styles

In addition to the previously mentioned analyses, in Fig. 6 we report the evolution of the angle between the vertical axis and the unit vector along the z-direction in the body frame. This measurement enabled us to quantify the angular variation during the motion of the objects. By incorporating this information, we were able to further validate and confirm the qualitative results obtained.

To complete the quantitative analysis, in figures 7 and 8 we present the body velocity profiles for the fluttering and tumbling modes, as they exhibit significant differences. During fluttering, the disc undergoes oscillations in the xy plane, symmetrical with respect to the vertical axis. This behavior is evident in the profiles of the translational velocities along the x and y axes, as they exhibit oscillations between two values of opposite signs. During tumbling instead, the disc tends to follow a unidirectional motion, losing any form of symmetry. As a result, the translational speed profiles do not change sign throughout the tumbling process. Additionally, during tumbling, the disc may experience a decrease in the average falling speed. This slowdown can be attributed to the center of gravity shifting its position along the positive z-axis direction due to autorotation.

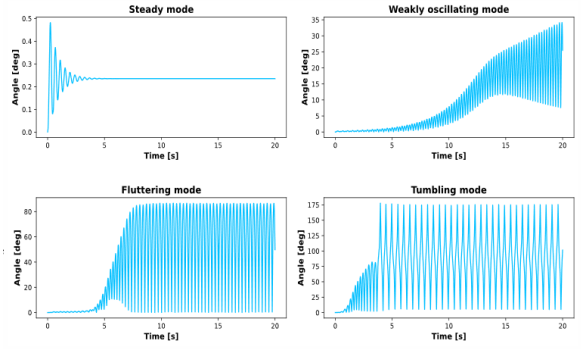

Figure 6: Angles variation in time

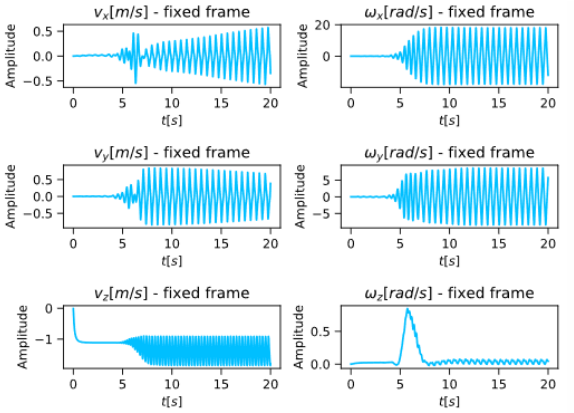

Figure 7: Fluttering - velocity variation in time

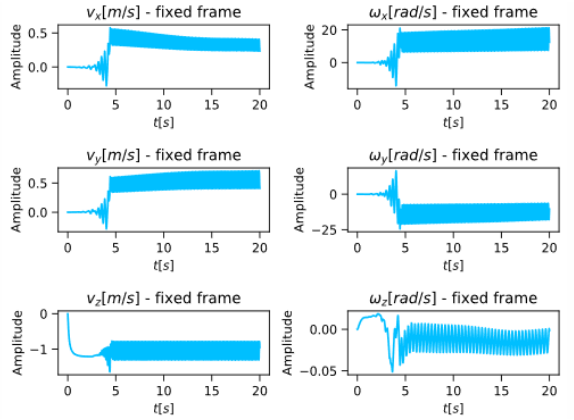

Figure 8: Tumbling - velocity variation in time

4 CONCLUSIONS

The primary aim of this study is to examine the main falling patterns displayed by symmetrical axial geometries, particularly discs with a diameter-to-thickness ratio exceeding 10. To achieve this objective, a combination of qualitative and quantitative analyses was employed. Qualitative analysis involved studying the trajectory of falling objects to identify the predominant modes. Additionally, quantitative measures such as the Strouhal number, angle variations

relative to the vertical axis, and speed profiles were utilized to provide a more comprehensive characterization of the identified modes. By employing these approaches, the study successfully distinguished and categorized the main modes of motion. Furthermore, the study introduces a definition of stabilization resulting from the piercing of the disk, adding to the understanding of the phenomenon. The results obtained in this study align with existing literature, both in terms of qualitative and quantitative observations. Additional simulations must be performed in order to better delineate the boundary in the phase diagram. Nevertheless, these findings lay a solid groundwork for further research and investigations in this field.

ACKNOWLEDGMENTS

We thank professor A. DeSimone for suggesting the problem and for useful discussions. We gratefully acknowledge the financial support of the European Commission through the FETPROACT-EIC-08-2020 Grant No. 101017940 (I-Seed). We are also grateful to CINECA for an award under the ISCRA initiative (B Grant MT-SWS21, C Grant IsCa4_I-seed) for the availability of high performance computing resources and support.

REFERENCES

[1] Mougin, G., & Magnaudet, J. (2002). The generalized Kirchhoff equations and their application to the interaction between a rigid body and an arbitrary time-dependent viscous flow. International journal of multiphase flow, 28(11), 1837-1851.

[2] Sigrist, J. F. (2015). Fluid-structure interaction: an introduction to finite element coupling. John Wiley & Sons.

[3] Chrust, M., Bouchet, G., & Dusek, J. (2013). Numerical simulation of the dynamics of freely falling discs. Physics of Fluids, 25(4), 044102.

[4] Field, S. B., Klaus, M., Moore, M. G., & Nori, F. (1997). Chaotic dynamics of falling disks. Nature, 388(6639), 252-254.

[5] Mortensen, M., & Valen-Sendstad, K. (2015). Oasis: a high-level/high-performance open source Navier–Stokes solver. Computer physics communications, 188, 177-188.

[6] Vincent, L., Shambaugh, W. S., & Kanso, E. (2016). Holes stabilize freely falling coins. Journal of Fluid Mechanics, 801, 250-259.

[7] Zhong, H., Chen, S., & Lee, C. (2011). Experimental study of freely falling thin disks: Transition from planar zigzag to spiral. Physics of Fluids, 23(1), 011702.

[8] Chrust, M., Bouchet, G., & Dusek, J. (2014). Effect of solid body degrees of freedom on the path instabilities of freely falling or rising flat cylinders. Journal of Fluids and Structures, 47, 55-70.

[9] Mittal, R., Seshadri, V., & Udaykumar, H. S. (2004). Flutter, tumble and vortex induced autorotation. Theoretical and Computational Fluid Dynamics, 17, 165-170.

[10] Willmarth, W. W., Hawk, N. E., & Harvey, R. L. (1964). Steady and unsteady motions and wakes of freely falling disks. The physics of Fluids, 7(2), 197-208.

[11] Alnæs, M., Blechta, J., Hake, J., Johansson, A., Kehlet, B., Logg, A., ... & Wells, G. N. (2015). The FEniCS project version 1.5. Archive of numerical software, 3(100).

[12] G. Corsi, G. Vagnoli, P.G. Ledda, F. Gallaire, A. De Simone (2023). Instability and trajectories of buoyancy-driven annular disks: a numerical study. In preparation.